nature chemistry

Article

https://doi.org/10.1038/s41557-024-01619-5

Shape-persistent ladder molecules exhibit nanogap-independent conductance in single-molecule junctions

Received: 15 October 2023

Accepted: 30 July 2024

Published online: 26 August 2024

Check for updates

Xiaolin Liu[1,2,6], Hao Yang[1,3,6], Hassan Harb[4,6], Rajarshi Samajdar[1,5], Toby J. Woods[2], Oliver Lin[2], Qian Chen[1,2,3], Adolfo I. B. Romo[1,2], Joaquín Rodríguez-López[1,2], Rajeev S. Assary[4] ✉, Jeffrey S. Moore[1,2,3] ✉ & Charles M. Schroeder[1,2,3,5] ✉

Molecular electronic devices require precise control over the flow of current in single molecules. However, the electron transport properties of single molecules critically depend on dynamic molecular conformations in nanoscale junctions. Here we report a unique strategy for controlling molecular conductance using shape-persistent molecules. Chemically diverse, charged ladder molecules, synthesized via a one-pot multicomponent ladderization strategy, show a molecular conductance ($d[\log(G/G_0)]/dx \approx -0.1\ nm^{-1}$) that is nearly independent of junction displacement, in stark contrast to the nanogap-dependent conductance ($d[\log(G/G_0)]/dx \approx -7\ nm^{-1}$) observed for non-ladder analogues. Ladder molecules show an unusually narrow distribution of molecular conductance during dynamic junction displacement, which is attributed to the shape-persistent backbone and restricted rotation of terminal anchor groups. These principles are further extended to a butterfly-like molecule, thereby demonstrating the strategy's generality for achieving gap-independent conductance. Overall, our work provides important avenues for controlling molecular conductance using shape-persistent molecules.

The miniaturization of electronic devices has led to substantial advances ranging from portable computing devices to high-speed communication and high-density data storage[1]. In recent years, the transistor density on silicon-based microchips has doubled approximately every two years in accordance with Moore's Law[2]. Although this empirical observation has held true for decades, physical size limitations are beginning to disrupt this trend[3]. Molecular electronics offer a potential path forward for the continued miniaturization of nano- and microelectronic devices[4]. Single-molecule junctions generally consist of a molecular bridge linked to two or more metal electrodes via terminal anchor groups (for example, thiol, amine or pyridine)[5]. Despite recent progress[6–9], achieving robust and controllable conductance in single-molecule junctions remains challenging due to the dynamic nature of molecular conformations that invariably fluctuate over operational timescales at ambient temperatures, destabilizing device performance and impacting reproducibility. When using standard microfabrication techniques, it is challenging to construct electrodes with sub-5 nm features tailored for specific molecules, which

[1]Beckman Institute for Advanced Science and Technology, University of Illinois Urbana-Champaign, Urbana, IL, USA. [2]Department of Chemistry, University of Illinois Urbana-Champaign, Urbana, IL, USA. [3]Department of Materials Science and Engineering, University of Illinois Urbana-Champaign, Urbana, IL, USA. [4]Materials Science Division, Argonne National Laboratory, Lemont, IL, USA. [5]Department of Chemical and Biomolecular Engineering, University of Illinois Urbana-Champaign, Urbana, IL, USA. [6]These authors contributed equally: Xiaolin Liu, Hao Yang, Hassan Harb. ✉e-mail: assary@anl.gov; jsmoore@illinois.edu; cms@illinois.edu

https://doi.org/10.1038/s41557-024-01619-5

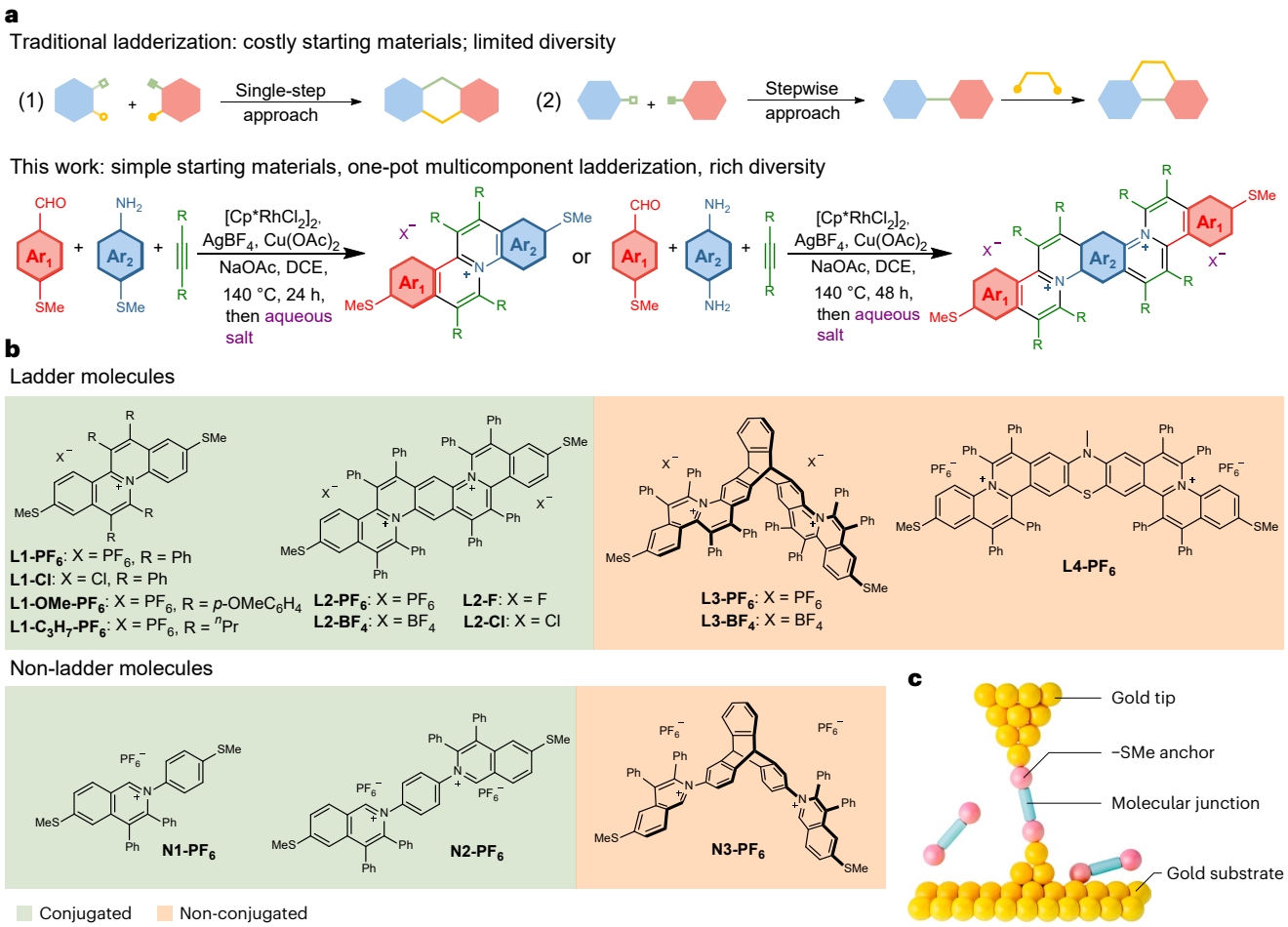

Fig. 1 | Molecular design and synthesis for single-molecule electronics. **a**, Comparison between traditional ladderization approaches (top) and the one-pot multicomponent ladderization method developed in this study (bottom). Cp*, pentamethylcyclopentadienyl; DCE, 1,2-dichloroethane. **b**, Chemical structures of the ladder molecules and their non-ladder counterparts. Ladders are denoted with an **L** and their non-ladder counterparts are denoted by **N**. **c**, Schematic representation of a molecular junction in the STM-BJ technique.

leads to distorted molecular conformations in nanoscale junctions[10,11]. Uncertainties in nanogap dimensions ultimately lead to unfavourable broad variations in molecular conductance[12].

Advances in molecular design offer promising strategies for controlling molecular conformations in nanoscale junctions. Molecules exhibiting a junction-conformation-independent conductance could overcome the limitations associated with precise control over nanogap dimensions and conformational variability. Ladder-type molecules feature an uninterrupted sequence of rings with two or more shared atoms between adjacent rings[13], which provides unique structural characteristics beneficial to molecular electronics[14,15]. Ladder molecules exhibit a shape-persistent architecture[16] that reduces the conformational degrees of freedom[17,18]. Moreover, ladder-type organic heteroaromatic cations are highly electron deficient[19] and can act as electron acceptors to endow the molecules with unique donor–acceptor charge transport properties[20]. With this in mind, we hypothesized that charged ladder-type molecules would exhibit a nanogap-independent conductance in single-molecule junctions—a trait seldom observed in conformationally flexible scaffolds[21]. In addition, the increased coplanarity in ladder-type molecules promotes delocalization of the frontier orbitals across the molecule[22,23], facilitating efficient end-to-end charge transport along the backbone.

Despite the potential advantages of using ladder molecules for molecular electronics, synthetic challenges have limited systematic exploration of the relationship between ladder structure and molecular conductance[24]. Traditional ladderization strategies primarily involve multistep one- or two-component reactions (Fig. 1a) that typically fuse two molecular rings (at most) per step[25–27]. In general, these synthetic approaches limit the structural and functional diversity of the ladder products. Therefore, continued advances in the field critically rely on the development of robust and scalable synthesis methods that accommodate a wide array of ladder configurations.

The electronic properties of single molecules can be experimentally characterized using the scanning tunnelling microscope break-junction (STM-BJ) technique[28–31]. The STM-BJ method is used to determine molecular conductance as a function of applied bias and junction displacement, providing statistically robust measurements by repeatedly forming and breaking junctions over a large ensemble of molecules in a single experiment (~10^3–10^4 molecules)[32]. The timescale of molecular conformational changes in an STM-BJ experiment (picoseconds to nanoseconds)[33] is typically orders of magnitude smaller than the timescale of a single STM-BJ trajectory (milliseconds)[34], suggesting that a broad range of molecular conformations is sampled over the course of a single 'pulling' experiment in STM-BJ. For these reasons, the conductance of individual molecules typically shows significant variability across the underlying ensemble[35–37], and average molecular conductance G is frequently reported along with one-dimensional (1D) conductance histograms in unit of G_0 where G_0 stands for the conductance quantum[21,38,39].

Here we adopt and expand a one-pot multicomponent ladderization approach to synthesize a diverse set of charged ladder molecules (Fig. 1b) bearing methylthio (−SMe) anchor groups for single-molecule electronic characterization. Our results demonstrate that ladder-type molecules with fused arene backbones exhibit a molecular conductance ($d[\log(G/G_0)]/dx \approx -0.1\ nm^{-1}$) that is independent of junction displacement x, in stark contrast to the nanogap-dependent conductance ($d[\log(G/G_0)]/dx \approx -7\ nm^{-1}$) for non-ladder analogues which exhibit large changes in molecular conductance. In addition, molecular conductance through the ladder backbone is robust and nearly independent of the chemical identities of counter anions or substituent groups. Our computational results show that charged ladder molecules exhibit constrained torsional motion in their terminal anchor groups, which contributes to an exceptionally narrow conductance distribution during dynamic 'pulling' trajectories in STM-BJ experiments. These results suggest that shape-persistent molecules with charged backbones give rise to donor–acceptor interactions that restrict anchor rotation, thereby minimizing conductance variation. We further demonstrate the broad applicability of shape persistence by designing, synthesizing and characterizing the electronic properties of a butterfly-like molecule, which also shows a nearly gap-independent conductance similar to that of ladder-type molecules. A combination of molecular simulations and chemical and physical characterization was used to understand the electronic properties of these molecules, including density functional theory (DFT) calculations, X-ray crystallography, electron paramagnetic resonance (EPR), superconducting quantum interfering device (SQUID) experiments and cyclic voltammetry. Overall, our work provides important avenues for achieving nanogap-independent conductance in molecular electronics using precise molecular design and synthesis.

Results and discussion

One-pot multicomponent synthesis

The C−H annulative coupling of benzaldehydes, anilines and alkynes catalysed by different co-catalysts ($[Cp^*RhCl_2]_2$, $Cu(OAc)_2$ and $AgBF_4$)[40] efficiently generates complex polycyclic aromatic hydrocarbons, including ladder molecules, in a highly adaptable and modular fashion. To evaluate the compatibility of the anchor group −SMe, we synthesized the short ladder molecule **L1-PF$_6$** from 4-(methylthio)benzaldehyde, 4-(methylthio)aniline and diphenylacetylene in 87% yield (Fig. 1b). Additional diarylalkyne and dialkylalkyne substrates were also efficiently tolerated in this multicomponent reaction. Post-annulation ion exchange reactions conveniently generated an expanded library of ladder compounds. Building on this success, we synthesized longer and more intricate ladders (for example, **L2-PF$_6$**, **L3-PF$_6$** and **L4-PF$_6$**) from dianilines or dialdehydes as starting materials, with yields ranging from 56% to 80%. The structures were extensively characterized by infrared spectroscopy (Supplementary Figs. 1–5), NMR spectroscopy (^{1}H and heteronuclear; Supplementary Figs. 6–62), high-resolution electrospray ionization mass spectrometry and single-crystal X-ray diffraction analysis (Supplementary Tables 1–3 and Supplementary Figs. 80–82). In addition to the facile installation of terminal anchor moieties for STM-BJ (Fig. 1c), this method provided a diverse array of ladders with adjustable backbones, pendent substituents and counter anions. Minor adjustments to the reaction conditions provided analogous non-ladder counterparts (for example, **N1-PF$_6$**, **N2-PF$_6$** and **N3-PF$_6$**), which served as unfused control molecules for single-molecule electronics experiments. The molecules are divided into four categories: conjugated ladder molecules (**L1** and **L2**), non-conjugated ladder molecules (**L3** and **L4**), conjugated non-ladder molecules (**N1** and **N2**) and a non-conjugated non-ladder molecule (**N3**).

Single-molecule electronics experiments

We characterized the single-molecule electronic properties of ladder and non-ladder molecules using the STM-BJ method[29,31]. In this experiment, a gold tip electrode is repeatedly moved into and out of contact with a gold substrate electrode in a solution containing molecules with terminal anchor groups, resulting in the repeated making and breaking of molecular junctions. During each molecular 'pulling' event, the current is measured for a constant applied bias across the molecular junction. The experiment begins as the tip moves away from the bottom (substrate) electrode, resulting in a sharp decrease in conductivity, typically observed at one unit of quantum conductance (G_0, where $G_0 = 2e^2/h$ or 77.5 μS; e, electron charge; h, Planck's constant), which indicates the start of the single-molecule pulling event. Molecular conductance is then measured as junction displacement increases, which corresponds to the formation of a single-molecule junction. At junction breakage, the molecular conductance abruptly decreases to the limit of detection of the instrument (~$10^{-5.5}G_0$). The STM-BJ instrument is automated, and the experiment is repeated over an ensemble of 10^3–10^4 molecules. Single-molecule conductance data are then analysed using 1D and two-dimensional (2D) histograms without data selection (Methods).

We determined 1D conductance histograms for ladder and non-ladder molecules (Fig. 2a). Conjugated ladder molecules **L1-PF$_6$** and **L2-PF$_6$** exhibited two dominant conductance peaks with high- and low-conductance features (vide infra). For the high-conductance peaks, the most probable or average conductance values for **L1-PF$_6$** and **L2-PF$_6$** were similar at $10^{-2.9}G_0$ and $10^{-3.2}G_0$, despite large differences in the end-to-end molecular contour length (12.5 Å for **L1-PF$_6$** and 18.0 Å for **L2-PF$_6$**, determined by DFT calculations). The attenuation factor for **L1-PF$_6$** and **L2-PF$_6$** (defined as the change in molecular conductance G/G_0 with respect to contour length) was determined to be 0.12 Å^{-1}, which can be compared to previously reported values for oligo[n]phenylenes[36] and oligothiophenes[41] (0.44 Å^{-1} and 0.40 Å^{-1}, respectively).

In contrast to the ladder molecules, the conjugated non-ladder molecules **N1-PF$_6$** and **N2-PF$_6$** showed significantly smaller average conductance values at $10^{-3.8}G_0$ and $10^{-4.8}G_0$, respectively. Moreover, the attenuation factor for conjugated non-ladder molecules **N1-PF$_6$** and **N2-PF$_6$** was observed to be 0.23 Å^{-1}, which is significantly larger than that of the conjugated ladder molecules **L1-PF$_6$** and **L2-PF$_6$**. These results highlight the role of the ladder structure in molecular junctions for achieving relatively high junction conductance levels and minimal conductance decays as a function of molecular contour length. In addition to the primary conductance peak at $10^{-4.8}G_0$, **N2-PF$_6$** also exhibits a small shoulder feature in the 1D conductance histogram around $10^{-3.2}G_0$, which is attributed to an intermediate junction conformation before the molecule is fully extended as suggested by 2D correlation analysis (Supplementary Fig. 68). The average conductance values of non-conjugated ladder molecules **L3-PF$_6$** and **L4-PF$_6$** were approximately $10^{-4.9}G_0$. The lack of conjugation within these molecules significantly lowers their average conductance values by nearly two orders of magnitude compared to **L2-PF$_6$**, which shows that continuous conjugation across the entire ladder structure significantly enhances molecular conductance. On the other hand, the non-conjugated, non-ladder molecule **N3-PF$_6$** exhibited a broad 1D conductance distribution, showing a peak value around $10^{-4.7}G_0$. Although 1D conductance histograms for **N3-PF$_6$** and **L3-PF$_6$** show similar peak conductance values, **N3-PF$_6$** showed conductance signals only at extremely small junction displacements around 0.2 nm (vide infra). These results arise because the characteristic conductance values of **N3-PF$_6$** at longer junction displacement distances fall below the limit of detection for the STM-BJ instrument.

In addition to the average conductance values, the width of the conductance distributions in 1D conductance histograms provides valuable insights into the electronic properties of molecular junctions. Broad conductance distributions often arise from variations in junction conformations, whereas narrow or tight conductance distributions typically indicate a more rigid or shape-persistent structure[21]. We determined the full-width at half-maximum (FWHM) of the primary

https://doi.org/10.1038/s41557-024-01619-5

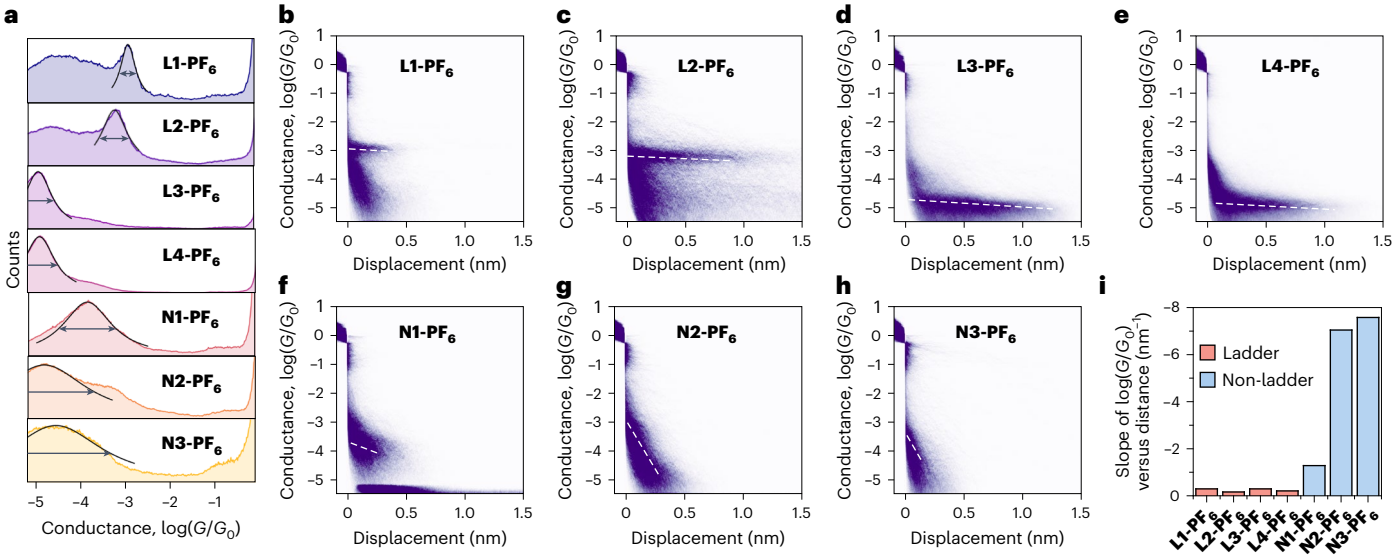

Fig. 2 | Single-molecule conductance of ladder and non-ladder molecules. **a**, 1D conductance histograms for ladder and non-ladder molecules. **b**–**h**, 2D conductance histograms for **L1-PF$_6$** (**b**), **L2-PF$_6$** (**c**), **L3-PF$_6$** (**d**), **L4-PF$_6$** (**e**), **N1-PF$_6$** (**f**), **N2-PF$_6$** (**g**) and **N3-PF$_6$** (**h**). A dashed white line shows a fit to the most probable conductance value as a function of junction separation (Methods). The colour scale of the heat map was standardized across all plots for comparison. **i**, Slopes derived from linear regression fits of the 2D conductance histograms in STM-BJ measurements. All data were obtained at 250 mV applied bias.

conductance peaks by fitting the 1D conductance histograms to a Lorentzian function[37]. For the ladder molecules (**L1-PF$_6$**, **L2-PF$_6$**, **L3-PF$_6$** and **L4-PF$_6$**), the FWHM was found to be $10^{0.41}$ (~2.6), $10^{0.69}$, $10^{0.75}$ and $10^{0.84}$ for the primary conductance peaks, respectively. By contrast, the non-ladder molecules (**N1-PF$_6$**, **N2-PF$_6$** and **N3-PF$_6$**) exhibited significantly broader conductance distributions with FWHM values of $10^{1.3}$, $10^{2.3}$ and $10^{2.5}$ (~316) for the primary conductance peaks, respectively. These results indicate that ladder-type molecules tend to have significantly narrower distributions in molecular conductance compared to non-ladder molecules. In addition, for both ladder and non-ladder molecules, the FWHM increases with molecular contour length, which suggests an increase in variation in the junction conformation for longer molecules.

Although 1D conductance histograms provide a convenient method to visualize single-molecule conductance distributions, peak conductance values may not fully reflect junction characteristics, particularly when conductance depends on molecular extension. To understand how molecular conductance depends on junction separation, we constructed 2D molecular conductance histograms by plotting conductance as a function of tip displacement (Fig. 2b–h). Ladder molecules exhibit remarkably constant conductance values during junction displacement (Fig. 2b–e and Supplementary Figs. 63–66). To quantitatively understand the variation in molecular conductance as a function of tip displacement, we determined the slope of trend lines fit to the peak conductance value as a function of junction displacement using linear regression (Fig. 2i and Methods). Our results show that the most probable conductance values of ladder molecules (**L1-PF$_6$**–**L4-PF$_6$**) exhibit extremely small changes in molecular conductance G/G_0 as a function of electrode separation x ($\mathrm{d}[\log(G/G_0)]/\mathrm{d}x \approx -0.1\ \mathrm{nm}^{-1}$), indicating the presence of robust and stable junctions with a nearly displacement-independent conductance. The nearly constant conductance during the junction elongation process suggests that the charge transport pathway is not disrupted, despite variations in molecular orientation or junction conformation inside the gap. The robust binding affinity between the –SMe group and gold atoms ensures that the anchor group and gold electrode remain in contact during the molecular pulling event until junction breakage[21,42]. Ladder-type molecules impart a rigid backbone that maintains the molecular conformation during junction displacement. This combination of anchor–electrode interactions and structural integrity within the molecule underpins the remarkable tolerance of conductance to junction displacement, highlighting a key design principle for the development of stable molecular electronics.

By contrast, non-ladder analogues (**N1-PF$_6$**–**N3-PF$_6$**) exhibit broadly distributed molecular conductance peaks spanning several orders of magnitude of conductance in the underlying ensemble (Fig. 2f–h). Non-ladder analogues (**N1-PF$_6$**–**N3-PF$_6$**) show much larger changes in molecular conductance as a function of junction displacement ($\mathrm{d}[\log(G/G_0)]/\mathrm{d}x \approx -7\ \mathrm{nm}^{-1}$). Besides the slope of the trend line, we also measured alpha values for **L1-PF$_6$** and **N1-PF$_6$**. Alpha value is an electromechanical property that reflects an intramolecular conductance decay measurement during which a sinusoidal function is applied during tip–substrate modulation[43] (more details in Supplementary Fig. 69). **L1-PF$_6$** exhibited a notably smaller alpha value of 0.6 nm^{-1}, in contrast to **N1-PF$_6$**, which presented an alpha value of 1.0 nm^{-1}. This finding indicates that the ladder molecule demonstrates a superior ability to maintain consistent conductance despite changes in junction distance.

In addition to the high-conductance peak, **L1-PF$_6$** and **L2-PF$_6$** also exhibited a less well-defined low-conductance peak. To understand the origin of these conductance features, we used a 2D correlation analysis of single-molecule conductance trajectories (Fig. 3a) that showed a negative correlation between the two molecular conductance populations, indicating that either one or the other conductance feature occurs in individual single-molecule traces. These results suggest that these two molecular conductance features arise due to different molecular junction conformations (static heterogeneity) rather than dynamic molecular junction conformations that interchange during the molecular pulling trajectory (dynamic heterogeneity). We further analysed the molecular conductance features of the ladder-type molecules using flicker noise analysis[34,44]. Flicker noise analysis provides a measure of conductance fluctuations that reveals information regarding molecular conduction pathways (for example, through-bond or through-space conductance)[32,40]. In this experiment, we performed holding-mode conductance measurements where molecular junctions were held at a fixed displacement for ~100 ms. Conductance traces

https://doi.org/10.1038/s41557-024-01619-5

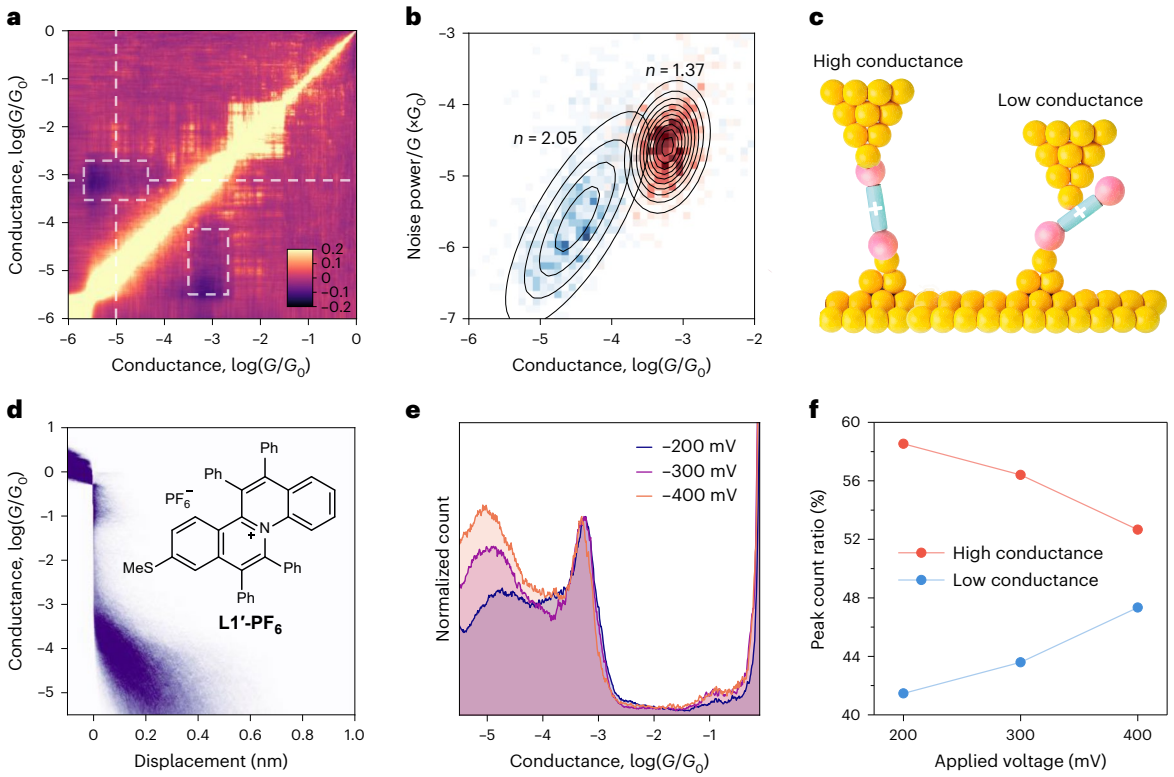

Fig. 3 | Voltage-regulated dual charge transport pathways in ladder molecules. a, 2D correlation analysis of the single-molecule conductance traces for **L2-PF$_6$**. The conductance feature centring around −3 log(G/G_0) is negatively correlated with the conductance feature centring around −5 log(G/G_0). **b**, Flicker noise analysis of molecular subpopulations corresponding to the high- and low-conductance features, respectively, for **L2-PF$_6$**, which suggests through-bond and through-space conductance pathways for the high- and low-conductance features (scaling exponents of $n \approx 1.37$ and $n \approx 2.05$, respectively). **c**, Schematic illustration of the junction conformations for ladder molecules, resulting in high- and low-conductance charge transport pathways. **d**, 2D conductance histogram for control molecule **L1′-PF$_6$** (inset) containing only one terminal −SMe anchor. **e**, 1D conductance histogram for **L2-PF$_6$** with different bias voltages applied between the gold tip and the substrate. The counts were normalized using high-conductance counts as the reference. **f**, Ratio of molecular conductance peak probability for high- and low-conductance states in **L2-PF$_6$**, as a function of applied bias.

surviving the holding period were then selected and their noise power was determined by integrating the conductance noise power spectral density in a frequency range from 100 Hz to 1,000 Hz (Methods), as previously reported[15]. Prior work has shown that the conductance tends to have smaller variations for through-bond conduction pathways[44]. On the other hand, fluctuations in conductance are typically larger for through-space conduction pathways, where chemical bonds do not cover the entire conduction pathway and electrons tunnel through space to complete the circuit. Prior work has shown that plotting normalized noise power (noise power/G^n) versus average normalized conductance G yields a power-law dependence where the scaling exponent $n \approx 1$ indicates a through-bond conduction pathway, whereas $n \approx 2$ indicates a through-space conduction pathway[44].

Before performing flicker noise analysis, we used the K-means++ clustering algorithm to classify single-molecule traces corresponding to high- and low-conductance features into two distinct molecular subpopulations[45]. We then analysed each molecular subpopulation using flicker analysis; the high-conductance feature resulted in a scaling exponent $n \approx 1.37$, consistent with a through-bond conductance pathway. By contrast, the low-conductance feature yielded a scaling exponent $n \approx 2.05$, consistent with a through-space conductance pathway (Fig. 3b). Based on these results, we hypothesized that the low-conductance feature arises from molecular junctions formed by electrostatic interactions between the gold tip and the positively charged backbone at one terminus and by the −SMe anchor and electrode surface at the other terminus (Fig. 3c). To validate this hypothesis, we synthesized a ladder molecule **L1′-PF$_6$** with only one terminal −SMe anchor group as a control and determined its conductance using STM-BJ. Indeed, the entire 2D conductance histogram of **L1′-PF$_6$** (Fig. 3d) was dominated by a low-conductance feature closely matching the low-conductance behaviour of **L2-PF$_6$**, which is consistent with the hypothesis of electrostatic anchor formation governing the low-conductance peak of **L2-PF$_6$**. We further studied the conductance of **L2-PF$_6$** as a function of an applied bias from 200 mV to 400 mV (Fig. 3e). With an increase in applied bias, our results show an increase in the probability of the molecular subpopulation corresponding to the low-conductance feature. This phenomenon is attributed to the voltage-dependent behaviour of electrostatic interactions forming junction contacts between the charged molecular backbone and the gold electrode[46]. Taken together, our results clearly demonstrate the ability to control the distribution between charge transport pathways simply by changing the applied bias (Fig. 3f).

Our multicomponent synthetic approach enables facile elucidation of the role of molecular substitutions, side groups and counter ions on molecular charge transport. Ladders bearing aromatic (C_6H_5, p-$OMeC_6H_4$) or aliphatic (^{n}Pr) groups exhibited similar average end-to-end conductance values corresponding to the high-conductance feature (Fig. 2b and Supplementary Fig. 64). Interestingly, the high-conductance feature remained nearly constant for **L2** regardless of the complexing anion (F^-, Cl^-, BF_4^- or PF_6^-; Supplementary Figs. 65 and 67). However, prior work reported that molecular charge transport in viologen-based molecules is highly dependent on the chemical identity of the counter ions[47]. DFT simulations showed that differences in conductance for viologen molecules were driven

https://doi.org/10.1038/s41557-024-01619-5

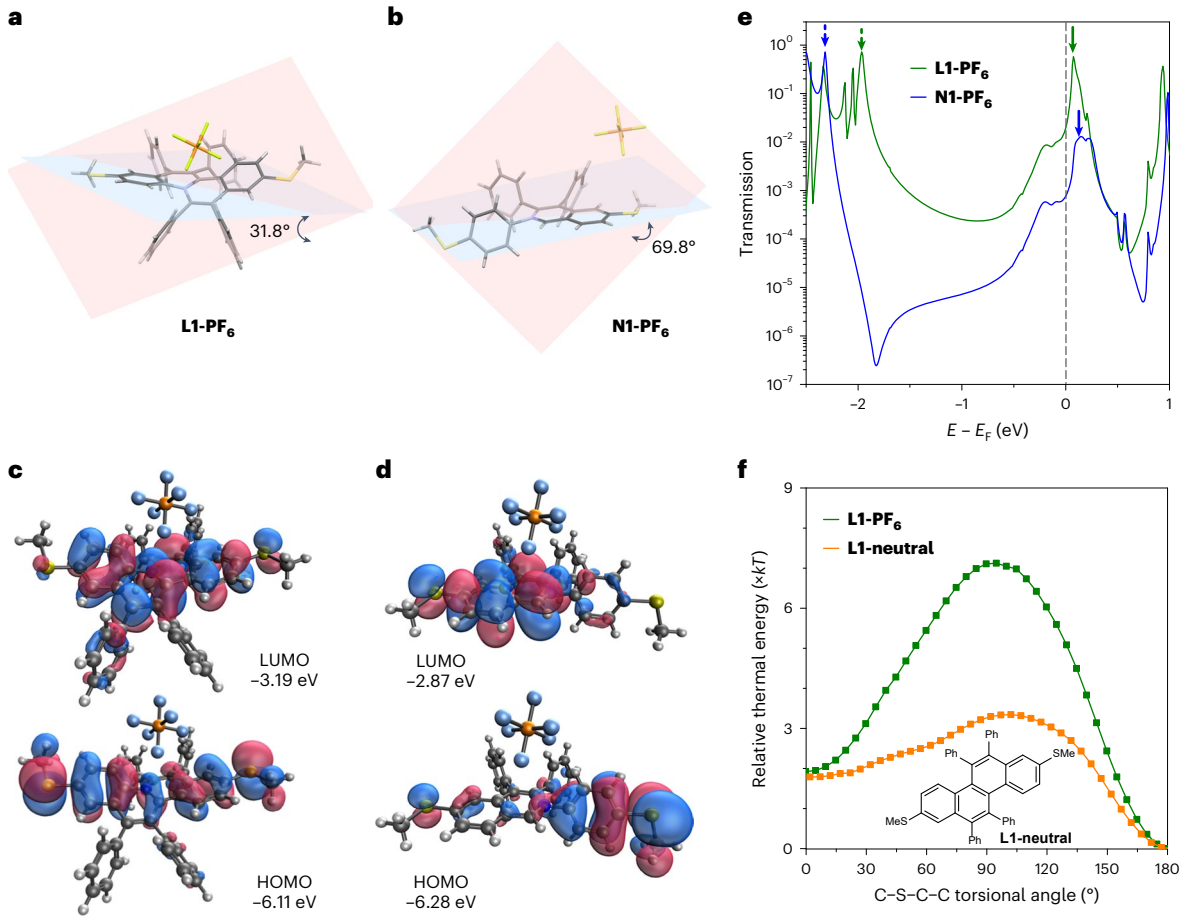

Fig. 4 | Comparative analysis of structural and electronic properties. **a**,**b**, Single-crystal structure of **L1-PF$_6$** (**a**) and **N1-PF$_6$** (**b**) determined by single-crystal X-ray diffraction. **c**,**d**, Molecular orbitals of **L1-PF$_6$** (**c**) and **N1-PF$_6$** (**d**) determined using DFT with B3LYP/6-311 + G(*d*,*p*). **e**, Transmission calculations for **L1-PF$_6$** and **N1-PF$_6$** as functions of energy *E* relative to the Fermi energy E_F from NEGF DFT simulations. **f**, Energy as a function of C–S–C–C torsional angle for **L1-PF$_6$** and its neutral analogue **L1-neutral** (shown in inset).

by changes in the torsion angles of the molecular backbone, which sensitively depend on counter anion identity[47]. Our results suggest that a shape-persistent structure minimizes the rotational degrees of freedom of the molecular backbone, and hence the junction conductance is independent of counter ion identity.

Structure and electronic properties

We further aimed to understand the physical and chemical origins of the conductance behaviour of ladder-type molecules. We first determined the single-crystal structures of **L1-PF$_6$** and **N1-PF$_6$** (Fig. 4a,b) by X-ray diffraction. The molecular backbone of non-ladder molecule **N1-PF$_6$** showed a large dihedral angle of 69.8° between phenyl and isoquinolinium moieties due to its non-ladder structure. Conversely, **L1-PF$_6$** with its shape-persistent ladder backbone exhibited a notably smaller dihedral angle of 31.8°. DFT calculations (Fig. 4c and Supplementary Figs. 83 and 84) revealed that in **L1-PF$_6$**, both the highest occupied molecular orbital (HOMO) and the lowest unoccupied molecular orbital (LUMO) span the entire molecule. This electronic configuration creates a seamless, unhindered pathway for electron transport while simultaneously constraining the backbone flexibility (Fig. 4c). On the other hand, the HOMO and LUMO of the **N1-PF$_6$** were localized on opposite ends of the rotatable C–N bond (Fig. 4d). In addition, all the ladder molecules showed a substantial bathochromic shift in the UV–visible absorption spectra (Supplementary Figs. 70–72) compared with their non-ladder counterparts, indicating enhanced conjugation arising from backbone coplanarity[48]. These apparent differences in the electronic and structural properties result in drastic differences in the single-molecule electronic properties for these two types of molecules.

We next performed transmission function calculations (Fig. 4e and Supplementary Figs. 85 and 86) for ladder and non-ladder molecules using the non-equilibrium Green's function (NEGF) method by employing the TranSIESTA/TBtrans package[49–51] (Methods). As shown in Fig. 4e, zero-bias transmission probabilities are plotted as a function of energy relative to the Fermi energy E_F, where HOMO and LUMO resonance transport peaks are denoted by dashed and solid arrows. For both **L1-PF$_6$** and **N1-PF$_6$**, the LUMO transmission peaks are located close to the Fermi energy level, which is consistent with a LUMO-dominated charge transport mechanism. This phenomenon was attributed to the highly electron-deficient nature of the positively charged backbones in both molecules. This electron deficiency was evidenced by cyclic voltammogram reduction events at −1.1 V and −1.5 V for **L1-PF$_6$** and **N1-PF$_6$**, respectively, using ferrocene as a reference (Supplementary Figs. 73 and 74). The transmission function probability at E_F for **L1-PF$_6$** is an order of magnitude larger compared to **N1-PF$_6$**, which is qualitatively consistent with the experimental data.

EPR (Supplementary Figs. 75–78) and SQUID (Supplementary Fig. 79) measurements provided additional evidence for electron delocalization in ladder molecules, which arises due to their locked molecular architecture. Electron delocalization is likely a key contributor to the observed high-conductance values and minimal conductance decay as the molecule length increases. Moreover, in contrast to **L1-PF$_6$**, **N1-PF$_6$** shows a pronounced anti-resonance dip (Fig. 4e) that is consistent with

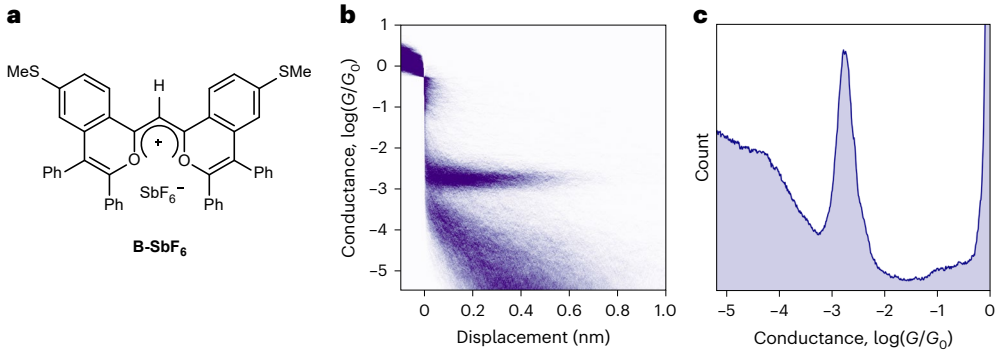

Fig. 5 | Single-molecule conductance of a butterfly-like molecule. a, Chemical structure of **B-PF$_6$**. **b**,**c**, 2D (**b**) and 1D (**c**) conductance histograms for **B-PF$_6$**.

destructive quantum interference, resulting in a diminished electron transmission probability and consequently leading to the suppression of molecular conductance[30,52].

Prior work[15,53] on ladder-type molecules with rigid backbones and –SMe anchors has not reported the well-defined conductance features observed here. Rigid molecular backbones generally show minimized structural variations compared to flexible molecular backbones. However, the ladder-type molecules studied here contain terminal anchor –SMe groups, which retain rotational degrees of freedom. We hypothesize that a donor–acceptor interaction between electron-deficient backbones and electron-rich –SMe anchors constrains anchor rotation by favouring specific angles[54], thus reducing variability in junction conductance. To test this hypothesis, we performed DFT calculations on a hypothetical neutral analogue molecule **L1-neutral** complemented by a dihedral angle sweep. The energy barrier for bond rotation in **L1-neutral** is approximately $3kT$, where k is the Boltzmann constant and T is temperature, but the barrier increases substantially to $>7kT$ for **L1-PF$_6$** (Fig. 4f). We further investigated the frontier orbitals corresponding to the dihedral angles at the highest and lowest energies. In the case of **L1-PF$_6$** (Supplementary Fig. 87), as the bond undergoes rotation from the lowest to the highest energy structure, a notable decrease in HOMO orbital overlap was observed between the –SMe anchor and the backbone. This observation implies that the anchor group engages in electron delocalization only at specific dihedral angles, subsequently restricting the rotational degrees of freedom. By contrast, **L1-neutral** (Supplementary Fig. 88), without the donor–acceptor interaction, exhibited a consistent frontier orbital structure, irrespective of the dihedral angle, suggesting a more uniform electron distribution behaviour. The constrained bond angle rotation in **L1-PF$_6$** minimizes junction structural variability, thereby refining the conductance distribution and yielding the distinctive sharp features observed in our 2D conductance histogram.

Broadly, our results suggest that shape-persistent molecular backbones together with donor–acceptor interactions effectively limit anchor rotation during junction elongation, which are key molecular features underlying gap-independent conductance. To demonstrate the broad applicability of these design principles, we explored an additional molecular system known as a butterfly-like molecule, **B-SbF$_6$** (Fig. 5a). The butterfly-like molecule exhibits a planar backbone[55], a feature attributed to electron delocalization rather than conventional covalent bonding to form a 'locked' backbone structure. The positively charged nature of the backbone serves as an effective electron acceptor, allowing for donor–acceptor interactions with the –SMe termini. Interestingly, the butterfly-like molecule shows a narrow conductance distribution across different junction gaps (Fig. 5b,c), which is similar to the behaviour exhibited by charged ladder-type molecules. These findings highlight an intriguing aspect of single-molecule junction design related to the degree of anchor rotation in addition to backbone rigidity.

Conclusions

Our work presents a molecular design strategy for molecular electronics that provides promising avenues for overcoming challenges associated with the fabrication of nanoscale devices with precise gap dimensions. Using a unique one-pot multicomponent synthesis strategy, we created a diverse range of positively charged ladder molecules from readily available starting materials. Our results show that charged ladder molecules exhibit exceptional shape-persistent conductance behaviour in molecular junctions, regardless of pendant substituent groups, counter anions or junction displacement. This conductance behaviour arises from both the rigidity of the ladder backbone and the constrained rotation of the anchor in charged systems. Importantly, we extend this design principle to a butterfly-like molecular system, showcasing our strategy's versatility for gap-independent conductance. Furthermore, the ladder structure promotes electron delocalization, enhancing conductance up to extremely high levels ($\sim 10^{1.6}$) compared to non-ladder counterparts. Interestingly, we further show that the probability of different binding sites can be controlled by varying the applied bias, which demonstrates control over dual charge transport pathways as a function of applied voltage. Overall, the innovative synthetic strategies and molecular design principles presented in this work highlight the role of charged ladder-type molecules as promising candidates for next-generation materials in the quest for miniaturization in electronic devices.

Online content

Any methods, additional references, Nature Portfolio reporting summaries, source data, extended data, supplementary information, acknowledgements, peer review information; details of author contributions and competing interests; and statements of data and code availability are available at https://doi.org/10.1038/s41557-024-01619-5.

References

1. Kim, J., Ghaffari, R. & Kim, D.-H. The quest for miniaturized soft bioelectronic devices. *Nat. Biomed. Eng.* **1**, 0049 (2017).
2. Lundstrom, M. Moore's law forever? *Science* **299**, 210–211 (2003).
3. Toumey, C. Less is Moore. *Nat. Nanotechnol.* **11**, 2–3 (2016).
4. Xiang, D., Wang, X., Jia, C., Lee, T. & Guo, X. Molecular-scale electronics: from concept to function. *Chem. Rev.* **116**, 4318–4440 (2016).
5. Meng, L. et al. Dual-gated single-molecule field-effect transistors beyond Moore's law. *Nat. Commun.* **13**, 1410 (2022).
6. Li, T., Bandari, V. K. & Schmidt, O. G. Molecular electronics: creating and bridging molecular junctions and promoting its commercialization. *Adv. Mater.* **35**, 2209088 (2023).
7. Chen, H. & Fraser Stoddart, J. From molecular to supramolecular electronics. *Nat. Rev. Mater.* **6**, 804–828 (2021).
8. Stone, I. et al. A single-molecule blueprint for synthesis. *Nat. Rev. Chem.* **5**, 695–710 (2021).

9. Zou, Q., Qiu, J., Zang, Y., Tian, H. & Venkataraman, L. Modulating single-molecule charge transport through external stimulus. *eScience* **3**, 100115 (2023).
10. Li, T., Hu, W. & Zhu, D. Nanogap electrodes. *Adv. Mater.* **22**, 286–300 (2010).
11. Luo, S., Hoff, B. H., Maier, S. A. & de Mello, J. C. Scalable fabrication of metallic nanogaps at the sub-10 nm level. *Adv. Sci.* **8**, 2102756 (2021).
12. Chang, S., He, J., Zhang, P., Gyarfas, B. & Lindsay, S. Gap distance and interactions in a molecular tunnel junction. *J. Am. Chem. Soc.* **133**, 14267–14269 (2011).
13. McNaught, A. D. & Wilkinson, A. *Compendium of Chemical Terminology* Vol. 1669 (Blackwell Science, 1997).
14. Cai, Z. et al. Exceptional single-molecule transport properties of ladder-type heteroacene molecular wires. *J. Am. Chem. Soc.* **138**, 10630–10635 (2016).
15. Li, J. et al. Ladder-type conjugated molecules as robust multi-state single-molecule switches. *Chem* **9**, 2282–2297 (2023).
16. Moore, J. S. Shape-persistent molecular architectures of nanoscale dimension. *Acc. Chem. Res.* **30**, 402–413 (1997).
17. Cao, Z., Leng, M., Cao, Y., Gu, X. & Fang, L. How rigid are conjugated non-ladder and ladder polymers? *J. Polym. Sci.* **60**, 298–310 (2022).
18. Ikai, T. et al. Triptycene-based ladder polymers with one-handed helical geometry. *J. Am. Chem. Soc.* **141**, 4696–4703 (2019).
19. Liu, X., Zhu, C. & Tang, B. Z. Bringing inherent charges into aggregation-induced emission research. *Acc. Chem. Res.* **55**, 197–208 (2022).
20. Wan, X., Li, C., Zhang, M. & Chen, Y. Acceptor–donor–acceptor type molecules for high performance organic photovoltaics – chemistry and mechanism. *Chem. Soc. Rev.* **49**, 2828–2842 (2020).
21. Li, Z. et al. Understanding the conductance dispersion of single-molecule junctions. *J. Phys. Chem. C* **125**, 3406–3414 (2021).
22. Ji, X. et al. Pauli paramagnetism of stable analogues of pernigraniline salt featuring ladder-type constitution. *J. Am. Chem. Soc.* **142**, 641–648 (2020).
23. Maekawa, T., Ueno, H., Segawa, Y., Haley, M. M. & Itami, K. Synthesis of open-shell ladder π-systems by catalytic C–H annulation of diarylacetylenes. *Chem. Sci.* **7**, 650–654 (2016).
24. Babel, A. & Jenekhe, S. A. High electron mobility in ladder polymer field-effect transistors. *J. Am. Chem. Soc.* **125**, 13656–13657 (2003).
25. Teo, Y. C., Lai, H. W. H. & Xia, Y. Synthesis of ladder polymers: developments, challenges, and opportunities. *Chem. Eur. J.* **23**, 14101–14112 (2017).
26. Lee, J., Kalin, A. J., Yuan, T., Al-Hashimi, M. & Fang, L. Fully conjugated ladder polymers. *Chem. Sci.* **8**, 2503–2521 (2017).
27. Cai, Z., Awais, M. A., Zhang, N. & Yu, L. Exploration of syntheses and functions of higher ladder-type π-conjugated heteroacenes. *Chem* **4**, 2538–2570 (2018).
28. Huang, C., Rudnev, A. V., Hong, W. & Wandlowski, T. Break junction under electrochemical gating: testbed for single-molecule electronics. *Chem. Soc. Rev.* **44**, 889–901 (2015).
29. Li, L. et al. Highly conducting single-molecule topological insulators based on mono- and di-radical cations. *Nat. Chem.* **14**, 1061–1067 (2022).
30. Liu, J., Huang, X., Wang, F. & Hong, W. Quantum interference effects in charge transport through single-molecule junctions: detection, manipulation, and application. *Acc. Chem. Res.* **52**, 151–160 (2019).
31. Su, T. A., Neupane, M., Steigerwald, M. L., Venkataraman, L. & Nuckolls, C. Chemical principles of single-molecule electronics. *Nat. Rev. Mater.* **1**, 16002 (2016).
32. Xu, B. & Tao, N. J. Measurement of single-molecule resistance by repeated formation of molecular junctions. *Science* **301**, 1221–1223 (2003).
33. Dantus, M., Bowman, R. M. & Zewail, A. H. Femtosecond laser observations of molecular vibration and rotation. *Nature* **343**, 737–739 (1990).
34. Feng, A. et al. σ–σ Stacked supramolecular junctions. *Nat. Chem.* **14**, 1158–1164 (2022).
35. Li, J. et al. Achieving multiple quantum-interfered states via through-space and through-bond synergistic effect in foldamer-based single-molecule junctions. *J. Am. Chem. Soc.* **144**, 8073–8083 (2022).
36. Lee, W. et al. Increased molecular conductance in oligo[*n*] phenylene wires by thermally enhanced dihedral planarization. *Nano Lett.* **22**, 4919–4924 (2022).
37. Yu, H. et al. Efficient intermolecular charge transport in π-stacked pyridinium dimers using cucurbit[8]uril supramolecular complexes. *J. Am. Chem. Soc.* **144**, 3162–3173 (2022).
38. Venkataraman, L., Klare, J. E., Nuckolls, C., Hybertsen, M. S. & Steigerwald, M. L. Dependence of single-molecule junction conductance on molecular conformation. *Nature* **442**, 904–907 (2006).
39. Yao, X., Sun, X., Lafolet, F. & Lacroix, J.-C. Long-range charge transport in diazonium-based single-molecule junctions. *Nano Lett.* **20**, 6899–6907 (2020).
40. Kadam, V. D. et al. Cascade C–H annulation reaction of benzaldehydes, anilines, and alkynes toward dibenzo[*a*,*f*] quinolizinium salts: discovery of photostable mitochondrial trackers at the nanomolar level. *Org. Lett.* **20**, 7071–7075 (2018).
41. Capozzi, B. et al. Length-dependent conductance of oligothiophenes. *J. Am. Chem. Soc.* **136**, 10486–10492 (2014).
42. Kamenetska, M. et al. Formation and evolution of single-molecule junctions. *Phys. Rev. Lett.* **102**, 126803 (2009).
43. Rascón-Ramos, H., Artés, J. M., Li, Y. & Hihath, J. Binding configurations and intramolecular strain in single-molecule devices. *Nat. Mater.* **14**, 517–522 (2015).
44. Adak, O. et al. Flicker noise as a probe of electronic interaction at metal–single molecule interfaces. *Nano Lett.* **15**, 4143–4149 (2015).
45. Stefani, D. et al. Conformation-dependent charge transport through short peptides. *Nanoscale* **13**, 3002–3009 (2021).
46. Chen, H. et al. Single-molecule charge transport through positively charged electrostatic anchors. *J. Am. Chem. Soc.* **143**, 2886–2895 (2021).
47. Li, J. et al. Reversible switching of molecular conductance in viologens is controlled by the electrochemical environment. *J. Phys. Chem. C* **125**, 21862–21872 (2021).
48. Yang, J. S.-J. & Fang, L. Conjugated ladder polymers: advances from syntheses to applications. *Chem* **10**, 1668–1724 (2024).
49. Brandbyge, M., Mozos, J.-L., Ordejón, P., Taylor, J. & Stokbro, K. Density-functional method for nonequilibrium electron transport. *Phys. Rev. B* **65**, 165401 (2002).
50. José, M. S. et al. The SIESTA method for *ab initio* order-*N* materials simulation. *J. Phys. Condens. Matter* **14**, 2745 (2002).
51. Papior, N., Lorente, N., Frederiksen, T., García, A. & Brandbyge, M. Improvements on non-equilibrium and transport Green function techniques: the next-generation TRANSIESTA. *Comput. Phys. Commun.* **212**, 8–24 (2017).
52. Bai, J. et al. Anti-resonance features of destructive quantum interference in single-molecule thiophene junctions achieved by electrochemical gating. *Nat. Mater.* **18**, 364–369 (2019).
53. Chen, Y. et al. Regio- and steric effects on single molecule conductance of phenanthrenes. *Nano Lett.* **21**, 10333–10340 (2021).

54. Gómez-Gallego, M., Martín-Ortiz, M. & Sierra, M. A. Concerning the electronic control of torsion angles in biphenyls. *Eur. J. Org. Chem.* **2011**, 6502–6506 (2011).
55. Yin, J. et al. Acyl radical to rhodacycle addition and cyclization relay to access butterfly flavylium fluorophores. *Nat. Commun.* **10**, 5664 (2019).

Methods

Synthesis

All synthetic procedures were performed under an argon atmosphere, using Schlenk techniques. The detailed procedures for the synthesis of ladder, non-ladder and butterfly-like molecules along with the corresponding characterization data are presented in Supplementary Information.

Conductance measurement and analysis

Single-molecule conductance measurements. Single-molecule conductance was measured using the STM-BJ technique[29]. Experiments used a custom-built STM-BJ set-up, as previously reported[15]. Gold substrates were prepared by evaporating 100 nm of gold onto polished Ted Pella atomic force microscopy specimen discs with an electron-beam evaporator. STM tips were prepared with 0.25 mm Au wire (99.998%, Alfa Aesar). Measurements were performed in a propylene carbonate solution at room temperature (22 °C). STM tips were coated with Apiezon wax to minimize the area exposed to polar solvents and to reduce the non-faradaic current. Single-molecule conductance data were acquired at a sampling rate of 40 kHz. During experiments, the STM tip is controlled by a piezoelectric micro-positioner to repeatedly form and break molecular junctions, and the current is recorded and analysed during this process. A variable-gain low-noise current amplifier (DLPCA-200 from Artisan Technology Group) was used to accurately convert current to voltage for data processing. Data were obtained across molecular ensembles of at least 5,000 molecules and collected and analysed without data selection. The 2D conductance histograms were determined by aligning single-molecule conductance traces relative to the junction formation point (denoted as 0 nm displacement); 2D conductance histograms were fit with linear regression trend lines to better visualize and demonstrate conductance evolutions during the pulling process of the STM-BJ experiments. To perform the linear regression fitting, the 2D conductance histograms were first transformed into 50 distinct 1D conductance histograms at equally spaced intervals of junction displacement, such that each of the 1D conductance histograms correspond to the conductance distribution at a particular junction displacement. The peak values were then determined for the 1D conductance distributions, and the peak values were used as data points for linear regression analysis, from which the line fitting can be constructed.

K-means++ clustering algorithm. We applied the K-means++ clustering algorithm to separate individual traces into distinct populations[45]. Each trace was segmented into a 30-by-30 bin, 2D histogram and a 100-bin, 1D histogram. The resulting data, encompassing both conductance and displacement information, were then binned into these histograms. The 30-by-30, 2D histogram was reshaped into a vector containing 900 elements. Upon adding the 100 elements from the 1D histogram, a 1,000-element feature vector was generated, encapsulating displacement and conductance data. The K-means++ clustering algorithm was then performed on these feature vectors to effectively distinguish between the high- and low-conductance features.

Flicker noise analysis. Flicker noise analysis was performed to distinguish between intramolecular and intermolecular charge transport modes. To perform this analysis, the conductance fluctuations were experimentally determined while holding molecular junctions at a fixed tip-to-substrate separation for 100 ms. The transient conductance response was then analysed using discrete Fourier transform to obtain the noise power spectral density. Flicker noise power is determined by numerically integrating the power spectral density between frequencies of 100 Hz to 1,000 Hz. The 2D flicker noise histograms are then determined based on the flicker noise power and the corresponding average conductance. The relationship between the noise power and the average conductance can be described based on a scaling factor n. By fitting the 2D flicker noise histogram with a 2D Gaussian, the scaling factor n is determined when the correlation between the noise power divided by G^n and the average conductance is minimized. A scaling factor of $n \approx 1$ indicates through-bond conductance, whereas a scaling factor of $n \approx 2$ indicates through-space conductance. Because our experiments on ladder-type molecules revealed two clear populations, we first used the K-means++ clustering algorithm to classify the data into two distinct subpopulations. Flicker noise analysis was then performed independently for each cluster[44].

DFT methods

Electronic structure calculations. All electronic structure calculations were performed using the Gaussian 16 software[56], employing the unrestricted form of the B3LYP[57–61] functional combined with the 6-311 + G(*d*,*p*) basis set[62]. Dispersion corrections were included via Grimme's empirical GD3 model[63]. To account for solvation effects, an implicit conductor-like polarizable continuum model was used with acetonitrile as the solvent model[64]. Molecular geometry optimization was performed, and the nature of the stationary point on the potential energy surface was confirmed by the absence of imaginary frequencies[65]. To address counter ion effects, calculations were performed in the presence of explicit PF_6^- ions. The quantity of PF_6^- ions included in each calculation was dependent on the charge of the molecule under study. Specifically, PF_6^- ions were added until the overall charge of the system was neutral, effectively mimicking the influence of counter ions. Molecular orbitals were generated with a contour value of 0.04 a.u. The PF_6^- ion was strategically positioned in close proximity to a nitrogen site prior to the optimization process as nitrogen atoms in analogous molecules are known to be sites for positive charge accumulation[22,47].

Analysis of dihedral angles. To explore the rigidity of the molecules, the dihedral angle variation of a C–S–C–C fragment was systematically investigated in both **L1-PF$_6$** and **L1-neutral**. A constrained optimization was carried out using the 'opt=modredundant' keyword in Gaussian, which allow for the geometry of the molecule to be optimized at each step while fixing the C–S–C–C dihedral angle at a specific value. The dihedral angle was varied in 36 steps, each of 5 degrees, resulting in a complete 180 degree rotation. For each step, the geometry of the molecule was optimized with the specified dihedral angle fixed at the current value in the scan, thus generating an energy profile associated with the rotation about the C–S–C–C dihedral angle.

NEGF DFT calculations. The NEGF DFT calculations were performed with a DFT-based NEGF approach using the TranSIESTA/TBtrans package[49–51]. The electrodes contain eight layers of 16 gold atoms each. The sulfur atoms in the ladder molecules were made to interact with the gold atoms using a trimer binding motif, as described in the literature[66]. Prior to transport calculations, geometry relaxation of the molecules was carried out using the generalized gradient approximation Perdew–Burke–Ernzerhof functional[67]. The SZP basis sets were used for all the gold atoms. DZP basis sets were used for carbon, hydrogen, sulfur, nitrogen, phosphorous and fluorine. Electrode calculations were carried out with a 4 × 4 × 50 k-mesh. The geometry relaxation was carried out using a 4 × 4 × 1 k-mesh, and was performed until all the forces were <0.05 eV Å^{-1}. After the junction was relaxed, the transport calculations were carried out using the TranSIESTA package with the same functionals, basis sets, pseudopotential and k-mesh as the geometry relaxation. TBtrans was used to carry out the NEGF calculations and to obtain electron transmission as a function of energy (relative to the Fermi energy level). NEGF calculations were carried out from −3 eV to 3 eV with 0.01 eV energy increments.

Data availability

All data supporting the findings of this study are available within this Article and its Supplementary Information. Crystallographic data for

structures reported in this Article have been deposited at the Cambridge Crystallographic Data Center (CCDC) under deposition numbers CCDC 2294843 (**N1-PF$_6$**), 2334051 (**L4-PF$_6$**) and 2334052 (**L1-PF$_6$**). Copies of the data can be obtained free of charge via https://www.ccdc.cam.ac.uk/structures/. Source data are provided with this paper. These data are also available via *figshare* at https://doi.org/10.6084/m9.figshare.26314444 (ref. 68).

Code availability

The data that support the findings were acquired using a custom instrument controlled by custom software (Igor Pro, Wavemetrics). The software is available from the corresponding authors upon reasonable request.

References

56. Frisch, M. et al. Gaussian 16, revision C.01 (Gaussian, Inc., 2019).
57. Becke, A. D. A new mixing of Hartree–Fock and local density-functional theories. *J. Chem. Phys.* **98**, 1372–1377 (1993).
58. Becke, A. D. Density-functional thermochemistry. I. The effect of the exchange-only gradient correction. *J. Chem. Phys.* **96**, 2155–2160 (1992).
59. Becke, A. D. Density-functional thermochemistry. II. The effect of the Perdew–Wang generalized-gradient correlation correction. *J. Chem. Phys.* **97**, 9173–9177 (1992).
60. Becke, A. D. Density-functional thermochemistry. III. The role of exact exchange. *J. Chem. Phys.* **98**, 5648–5652 (1993).
61. Becke, A. D. Density-functional thermochemistry. IV. A new dynamical correlation functional and implications for exact-exchange mixing. *J. Chem. Phys.* **104**, 1040–1046 (1996).
62. Krishnan, R., Binkley, J. S., Seeger, R. & Pople, J. A. Self-consistent molecular orbital methods. XX. A basis set for correlated wave functions. *J. Chem. Phys.* **72**, 650–654 (2008).
63. Grimme, S., Antony, J., Ehrlich, S. & Krieg, H. A consistent and accurate *ab initio* parametrization of density functional dispersion correction (DFT-D) for the 94 elements H-Pu. *J. Chem. Phys.* **132**, 154104 (2010).
64. Barone, V. & Cossi, M. Quantum calculation of molecular energies and energy gradients in solution by a conductor solvent model. *J. Phys. Chem. A* **102**, 1995–2001 (1998).
65. Hratchian, H. P. & Schlegel, H. B. in *Theory and Applications of Computational Chemistry* (eds Dykstra, C. E. et al.) 195–249 (Elsevier, 2005).
66. Brisendine, J. M. et al. Probing charge transport through peptide bonds. *J. Phys. Chem. Lett.* **9**, 763–767 (2018).
67. Perdew, J. P., Burke, K. & Ernzerhof, M. Generalized gradient approximation made simple. *Phys. Rev. Lett.* **77**, 3865–3868 (1996).
68. Liu, X. et al. Shape-persistent ladder molecules exhibit nanogap-independent conductance in single-molecule junctions. *figshare* https://doi.org/10.6084/m9.figshare.26314444 (2024).

Acknowledgements

This research was supported by the US Department of Energy (DE-SC0022035). We express our gratitude to the Mass Spectrometry Laboratory and the 3M Materials Chemistry Laboratory at the University of Illinois for their assistance with mass spectrometry and X-ray experiments, respectively. Major funding for the 500 MHz Bruker CryoProbe was provided by the Roy J. Carver Charitable Trust (Muscatine, Iowa; grant no. 15-4521) to the School of Chemical Sciences NMR Lab. R.S.A. and H.H. acknowledge Laboratory Directed Research and Development (LDRD) funding from Argonne National Laboratory, provided by the Director, Office of Science, of the US Department of Energy under contract no. DE-AC02-06CH11357. H.H. and R.S.A. acknowledge the computing resources provided on 'BEBOP' and 'IMPROV', two computing clusters operated by the Laboratory Computing Resource Center at Argonne National Laboratory. X.L. acknowledges Y. Diao at the University of Illinois Urbana-Champaign for offering the use of the UV–visible spectrophotometer. X.L. acknowledges N. Jackson, B. A. Suslick and R. Zhang at the University of Illinois Urbana-Champaign for constructive suggestions.

Author contributions

X.L. and H.Y. conceived the idea, designed the experiments and wrote the paper. C.M.S., J.S.M. and R.S.A. co-supervised the project and revised the paper. X.L. designed and synthesized the molecules and conducted structural, optical and magnetic property and redox activity characterizations and analyses. H.Y. performed the break-junction experiments and analyses. H.H. carried out electronic structure calculations. R.S. carried out transmission calculations. T.J.W. performed single-crystal characterizations and analyses, and also provided technical guidance for EPR measurements. O.L. and Q.C. contributed constructive discussions. A.I.B.R. and J.R.-L. provided technical guidance for the cyclic voltammetry measurements.

Competing interests

The authors declare no competing interests.

Additional information

Supplementary information The online version contains supplementary material available at https://doi.org/10.1038/s41557-024-01619-5.

Correspondence and requests for materials should be addressed to Rajeev S. Assary, Jeffrey S. Moore or Charles M. Schroeder.

Peer review information *Nature Chemistry* thanks Daniel Paley and the other, anonymous, reviewer(s) for their contribution to the peer review of this work.